ORIGINAL RESEARCH

Beyond Chemistry: Investigating the Physical, Pharmacological, and Computational Aspects of Polyoxometalate Integrated Solid Lipid Nanoparticles for Cancer Treatment

Riffat Khan[1], Ume Ruqia Tulain [ID][1], Hamid Saeed Shah [ID][2], Faisal Usman[3], Tahir Ali Chohan[2], Jamshed Iqbal[4], Mohsin Kazi [ID][5], Muhammad Ijaz [ID][6,7], Alia Erum[1], Nadia Shamshad Malik [ID][8], Arshad Mahmood[9,10]

[1]Faculty of Pharmacy, University of Sargodha, Sargodha, 40100, Pakistan; [2]Institute of Pharmaceutical Sciences, University of Veterinary and Animal Sciences, Lahore, 54000, Pakistan; [3]Department of Pharmaceutics, Faculty of Pharmacy, Bahauddin Zakariya University, Multan, 66000, Pakistan; [4]Centre for Advanced Drug Research, COMSATS University Islamabad, Abbottabad Campus, Abbottabad, 22060, Pakistan; [5]Department of Pharmaceutics, College of Pharmacy, King Saud University, Riyadh, 11451, Saudi Arabia; [6]Department of Pharmacy, COMSATS University Islamabad, Lahore Campus, Lahore, Pakistan; [7]School of Veterinary Medicine, University College Dublin, Belfield, Dublin, D04 V1W8, Ireland; [8]Faculty of Pharmacy, Capital University of Science and Technology, Islamabad, Pakistan; [9]College of Pharmacy, Al-Ain University, Abu Dhabi Campus, Abudhabi, United Arab Emirates; [10]AAU Health and Biomedical Research Center, Al Ain University, Abu Dhabi, United Arab Emirates

Correspondence: Ume Ruqia Tulain; Muhammad Ijaz, Email umeruqia.tulain@uos.edu.pk; drmijaz@cuilahore.edu.pk

Purpose: The solid lipid nanoparticles of transitional metal complexes (POMs) were prepared with natural lipids with the aim of developing a safer therapeutic approach for cancer treatment.

Methods: Natural lipids were used to create solid lipid nanoparticles containing transitional metal complexes (POMs).

Results: The nanoparticles had displayed appreciable entrapment and loading percentage of P_5W_{30}. The zeta capacitance was measured to be -32.57 ± 6.44 mV with average particle dimension of 160.5 ± 8.61 nm and polydispersity index (PDI) of around 0.3814 ± 0.096. The effectiveness of P_5W_{30}-BW-SLNs in inhibiting the growth of HeLa cells was found to be higher ($IC_{50} = 3.02 \pm2.14$ μg/mL) compared to pure P_5W_{30} ($IC_{50} = 7.93\pm5.08$ μg/mL). Further examinations of DNA damage were made through comet test and flow cytometry techniques. The assessment of tumor regression and survival was conducted, and comparison was recorded. The P_5W_{30}-BW-SLNs resulted in a 72.91% increase in survival rates and a reduction in tumor burden by $2.967\pm0.543\%$. Moreover, the computational findings demonstrate a strong connection with the actual data, providing a plausible explanation for the notable chemopreventive efficacy of POM against HeLa cell lines.

Conclusion: The study's findings might pave the way for a more efficient delivery system in cancer treatment.

Keywords: polyoxometalate, beeswax, nanoparticle, molecular docking

Introduction

Polyoxometalates (POMs) are a fascinating group of inorganic clusters consisting of early transition metals, such as vanadium ($Na_6[H_2V_{10}O_{28}]\cdot18H_2O$), molybdenum $[NH_3Pri]6[Mo_7O_{24}]\cdot3H_2O$ (PM-8), and tungsten $(NH_4)_{14}[NaP_5W_{30}O_{110}]\cdot31H_2O$ (P_5W_{30}), that are linked together by oxygen atoms.[1] Polyoxometalates (POMs) like P5W30 are metal-oxide clusters with many uses in fields as diverse as medicine, materials research, and catalysis. Because of its exceptional structural and electrical characteristics, which provide substantial benefits for medicinal and drug delivery applications. These intricate structures, which have a resemblance to small molecular cages, have unique chemical, physical, and pharmacological properties.[2] Polyoxometalates (POMs) have become very prospective competitors in the realm of medicinal chemistry because of their favorable pharmacological characteristics, especially in relation to their potential use in anticancer treatments.[3,4]

Graphical Abstract
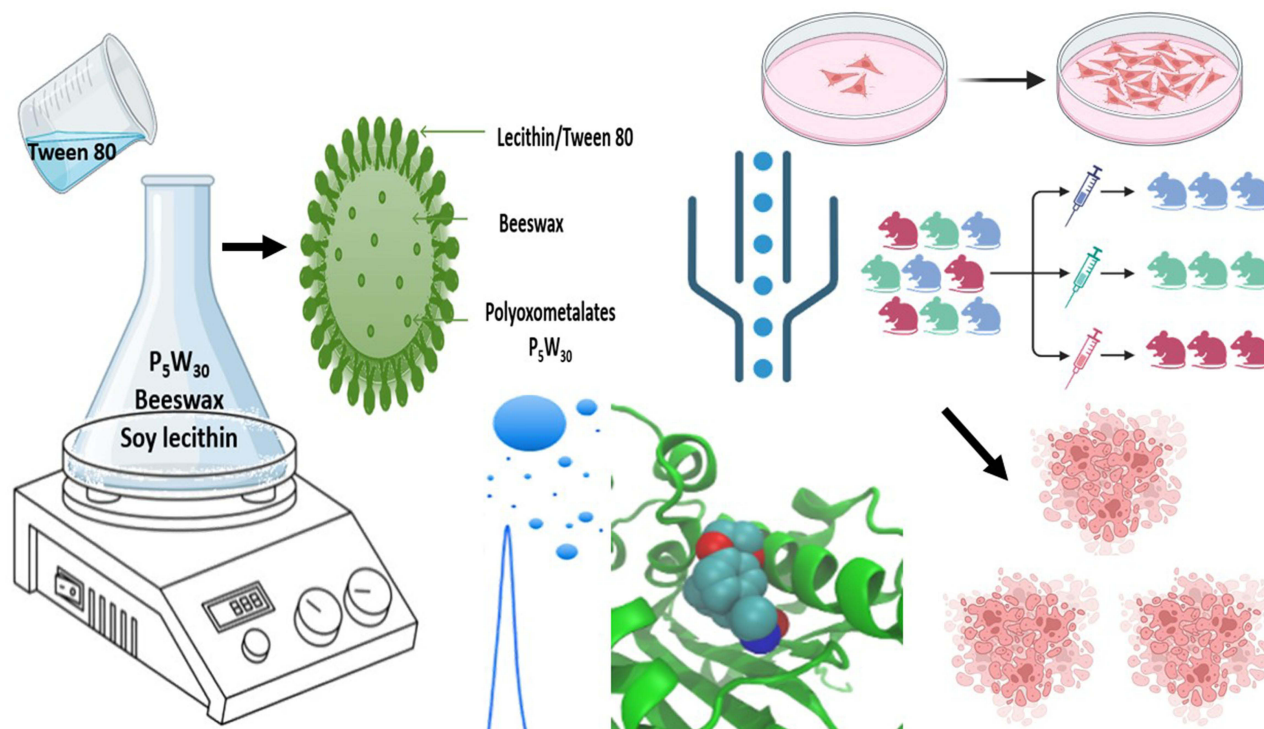
Polyoxometalates (POMs) are known to play a crucial role in fighting cancer by triggering apoptosis, which is the controlled death of cancer cells.[5] Polyoxometalates (POMs) have the ability to engage with cellular constituents and interfere with crucial processes that are vital for the survival of cancer cells, resulting in their targeted eradication.[6,7] Moreover, the redox characteristics of POMs allow them to regulate the levels of oxidative stress in cancer cells, so adding to their deadly effects.[8] Furthermore, Polyoxometalates (POMs) have shown promise as agents that limit angiogenesis, which is the process of forming new blood vessels that are essential for the development of tumors.[9] Their ability to inhibit the growth of blood vessels, known as anti-angiogenic property, highlights their effectiveness in slowing down the advancement of cancer.[10]

Although polyoxometalates (POMs) show potential as anticancer agents, their transformation into effective pharmaceuticals is hindered by various constraints.[11] A significant obstacle is their restricted solubility in water-based settings, which may hinder their capacity to be absorbed by the body and their effectiveness in treating medical conditions.[12]

The integration of water-insoluble metal complexes into solid lipid nanoparticles (SLNs) has considerable potential for therapeutic applications, particularly in the field of drug delivery.[13] Several metal complexes with significant therapeutic qualities, such as anticancer or antibacterial medicines, often encounter the drawback of low solubility, which restricts their practical use in clinical settings.[14] SLNs provide a smart solution by using a biocompatible lipid-based structure to enclose hydrophobic metal complexes, hence improving their solubility and stability.[15] This formulation enhances medication bioavailability and enables precise and prolonged release, hence increasing therapeutic effectiveness.[16] Moreover, SLNs can enhance precise distribution to certain tissues or cells, hence reducing the occurrence of systemic adverse effects.[13] The use of SLNs containing water-insoluble metal complexes has significant implications in the development of safer and more efficient therapies for a range of ailments.[17]

Beeswax, a lipid obtained from honeybees, is important in solid lipid nanoparticles (SLNs) because it is biocompatible and has minimal toxicity.[18] The incorporation of the substance improves the stability and controlled release characteristics of solid lipid nanoparticles (SLNs), leading to extended circulation of the medication and enhanced

therapeutic results. The versatile nature of beeswax, acting as a lipid matrix, facilitates the encapsulation of hydrophobic medicines, hence playing a crucial role in the creation of effective and secure drug delivery systems.[19] Furthermore, its sustainable and renewable characteristics are in line with the increasing focus on green formulations in the field of pharmaceuticals.[20]

The process entails constructing three-dimensional structures of the molecules, optimizing energy, and producing numerous binding positions. This approach is crucial in the field of drug development as it allows for the identification of possible drug candidates, comprehension of binding processes, and assistance in the design of drugs based on their structure. Molecular docking is a valuable tool in the field of cancer treatment using polyoxometalate (POM) integrated solid lipid nanoparticles. It aids in improving drug delivery, ensuring precise targeting, and gaining a better understanding of the mechanisms behind the anticancer effects of POMs. This, in turn, contributes to the advancement of nanomedicine therapies that are more effective.

This work included the preparation and characterization of solid lipid nanoparticles (SLNs) containing P_5W_{30}. The P_5W_{30} was chosen as the typical polyoxymethylene (POM) in our investigation because of its outstanding stability, solubility, and capacity to interact with biological systems in a regulated way. Due to its structural features, it is highly suitable for being included in solid lipid nanoparticles (SLNs) to achieve targeted distribution and enhance therapeutic effectiveness. The physical and in vitro pharmacological activities on HeLa cells of these P_5W_{30} incorporated SLNs were assessed. Eventually, the obtained results were validated by experimentation on animals. Furthermore, in silico simulations which aids in improving drug delivery, ensuring precise targeting, and gaining a better understanding of the mechanisms behind the anticancer effects of POMs. This, in turn, contributes to the advancement of nanomedicine therapies that are more effective.

Materials and Methods
Materials
Beeswax (BW), Soy lecithin (SL), Tween 80, Polyoxotungstate $((NH_4)_{14}[NaP_5W_{30}O_{110}]\cdot31H_2O))$ (P_5W_{30}), Sulforhodamine B (SRB) dye, MTT dye (3-(4,5-Dimethylthiazol-2-yl)-2,5-Diphenyltetrazolium Bromide), Tris base (pH 10.5), 4.6–Diamidino–2–phenylindole dihydrochloride (DAPI), Phosphate-buffered saline (PBS) tablets, Ethylenediaminetetraacetic acid (EDTA), Low melting point agarose (LMPA), Sodium hydroxide (NaOH), Sodium chloride (NaCl), Annexin–V–FITC, Trypsin, staining kit, Chloroform, Lactose, Fetal bovine serum (FBS), Ethanol, Trichloroacetic acid (TCA), Dulbecco's modified Eagle's medium (DMEM), Dimethyl sulfoxide (DMSO), Dialysis membrane (MWCO = 10K Da), Triton X–100 and phosphate-buffer tablets (pH 7.4) were acquired from Sigma Aldrich (St. Louis, MO, USA). These compounds were utilized without further purification. Furthermore, the Vero cell line (kidney tissue derived from a normal, adult African green monkey, CCL-81) and HeLa cells were acquired from ATCC, Japan).

Methods
Preparation of SLNs
The preparation of solid lipid nanoparticles (SLNs) was conducted using the microemulsion approach as described in a recent study.[21] The designated quantities (see Table 1) of a blend consisting of BW, SL, and POM (P_5W_{30}) were liquefied using a water bath heated to a temperature of 90°C. Tween 80 was combined with deionized water at

Table 1 Experimental Conditions for Preparation of Solid Lipid Nanoparticles (SLNs)

	F1-P_5W_{30}-BW-SLNs	F2-P_5W_{30}-BW-SLNs	F3-P_5W_{30}-BW-SLNs
Beeswax (g)	5	5	5
POMs (g)	0.5	0.5	0.5
Soy lecithin (g)	0	5	10
Tween 80	10	5	0

a temperature of 90°C and a rotational speed of 2000 rpm for a duration of 2 min, and then introduced into the molten lipid mixture kept at 90°C. The resultant optically clear system was disseminated at a speed of 24,000 rpm within a time frame of 5 min utilizing a rotor-stator (Ultra-Turrax, IKA T18 basic; Staufen, Germany). Ultimately, the microemulsion was slowly distributed in water chilled to a temperature of 2–4°C, with a volume ratio of 1:10, while stirring at a speed of 3000 rpm.

Physical Characterization

FTIR Spectroscopy

The BW, P_5W_{30}, and P_5W_{30}-BW-SLN spectra were acquired through the utilization of the KBr disc method.[22] To create the KBr disc, a sample was combined with 2% KBr powder. The Nicolet Avatar 370 FTIR spectrophotometer was utilized for collecting an FTIR spectrum encompassing the frequency range of 4000 to 400 cm^{-1}.

DSC Studies

To assess the physical integrity of the P_5W_{30} in SLNs, thermal analysis was conducted on BW, P_5W_{30}, and P_5W_{30}-BW-SLNs.[23] The heating rate was adjusted to 10°C/min while maintaining a constant flow of nitrogen (2 mL/min) to prevent oxidation. The DSC scan for each sample was recorded using a DSC 214 Polyma-NETZSCH (GmbH Germany) instrument, by heating it up to 350°C. An emptied aluminum pan served as a reference.

Percent Entrapment and Loading Efficiency

The drug loading efficiency (LE) along with drug encapsulation effectiveness (EE) of P_5W_{30} in BW-SLNs were determined by centrifuging the colloidal samples, containing a 2g BW-SLNs (equal to 30.76 mg P_5W_{30}), using a Hettich EBA 200S centrifuge at a speed of 18,000 rpm (39,846×g) for 15 min at a temperature of 25°C. The unentrapped P_5W_{30} in the supernatant obtained by centrifuging the SLNs was quantified using UV-visible spectroscopy at a specific wavelength of 241 nm (Shimadzu UV 1900i, Tokyo, Japan).[24] Prior to evaluating the drug concentration, we conducted UV-visible spectroscopy on the dispersion of Solid Lipid Nanoparticles (SLNs) to quantify the absorbance associated with the SLNs. The absorbance result was subtracted from the total absorbance obtained in the supernatant comprising both the drug and solid lipid nanoparticles (SLNs).

To calculate the percentage of P_5W_{30} that is enclosed inside nanoparticles, the difference between the total amount of P_5W_{30} used and the amount of unbound P_5W_{30} found in the aqueous phase of the supernatant was divided by the total amount of P_5W_{30} used. The LE (%) was computed by dividing the difference by the total weight of SLNs using the given calculations.

$$EE(\%) = \frac{Total\ P5W30\ added - P5W30\ in\ supernatant}{Total\ P5W30\ added} \times 100$$

$$LE(\%) = \frac{Total\ amount\ of\ P5W30\ added\ into\ SLNs}{Total\ amount\ of\ SLNs}$$

Hydrodynamic Dimension and Zeta Potential Measurement

To ascertain the hydrodynamic size of P_5W_{30}-BW-SLNs, the nanoparticles underwent several dispersion techniques using purified water. The particle sizes and zeta potential were analyzed using the Malvern Zetasizer Nano ZS (Cambridge, UK).[25]

Drug Release and Kinetics

The objective of this study is to determine kinetic models utilizing a pre-existing approach to analyze the release pattern of P_5W_{30} from BW-SLNs.[22] To summarize, a 2g of P_5W_{30}-BW-SLNs were combined with 5 mL of phosphate-buffered saline at a pH of 7.4. Afterward, the mixture was transferred into a dialysis bag with a molecular weight cut off (MWCO) of 10K Da. The dispersion containing the membrane pocket was then submerged in a solution of 500 mL of phosphate-buffered saline with a pH of 7.4. The system rotated at a frequency of 75 rpm at a temperature of 37°C. The release of P_5W_{30} was estimated on UV-visible spectrophotometer (Shimadzu UV 1900i, Tokyo, Japan) operated at a wavelength of

241 nm. Mathematical representations using release kinetics were employed to P_5W_{30} to verify the mechanism by which P_5W_{30} was discharged from BW-SLNs. The implementation of these models was carried out utilizing the DDsolver program.

Transmission Electron Microscopic Assessment

The morphology of P_5W_{30}-BW-SLNs (10 µL) was analyzed through the technique of transmission electron microscopy (TEM; JEM-2100; JEOL; Tokyo, Japan; 200 kV). Before imaging, the samples were treated using 2% uranyl acetate solution (w/v) to create a negative stain. The samples were then dried for 20 min. Afterward, the desiccated samples were positioned on a copper grid coated with carbon with an aperture size of 300.[26]

Scanning Electron Microscopy (SEM)

The SEM investigation was conducted using the Hitachi S–4700 (Hitachi, Ltd. Tokyo Japan). SEM apparatus, with an acceleration voltage ranging from 10 to 20 kV. The P_5W_{30}-BW-SLNs were dispersed using ethanol and immediately applied onto pristine silicon wafers. The samples underwent sputter-coating with gold to facilitate conduction.[27]

Pharmacological Assessment

Cytotoxicity and Cell Viability Assays

An SRB investigation was used to compare and assess the inhibitory effects on cell growth of pure P_5W30 and P_5W_{30}-BW-SLNs on the HeLa cell line.[28] A total of 10,000 cells were distributed evenly in 96-well plates and provided 24 hr to multiply. The distinct wells were subjected to different quantities of both P_5W_{30} and P_5W_{30}-BW-SLNs. After the cells were incubated, they were washed with PBS, allowed to dry naturally, and then fixed with 40% chilled trichloroacetic acid (TCA). The cells were treated with a 0.4% w/v solution of SRB dye for a duration of 30 min. The cells were then exposed to a 100 µL solution incorporating tris-base (10 mm, pH 10.5). The ELx808TM microplate reader (BioTek instruments Vermont, USA) was used to get readings at a wavelength of 565 nm. The IC_{50} value (µg/mL) was determined using Prism 5.0 software (GraphPad Software; California, USA).

To assess the effect of P_5W_{30} and P_5W_{30}-BW-SLNs on the survival of Vero cell line (a healthy adult African green monkey's kidneys, CCL-81, ATCC, Japan), a previously established MTT test was used with slight modifications.[29] All wells were seeded with 10,000 Vero cells and allowed to incubate for 24 hr for growth and proliferation. The cells were then subjected to varying doses of P_5W_{30} and P_5W_{30}-BW-SLNs. The duration of the treatment was extended for 48 hr. Following the treatment time, the cells were subjected to MTT and incubated in a light-restricted environment at a constant temperature of 37°C for a duration of 3–4 hr. As incubation time ended, the dark purple crystals of formazan emerged and were dispersed in isopropanol. The ELx808TM (BioTek instruments Vermont, USA), was utilized to get measurements at a wavelength of 565 nm.

DAPI Staining

A sterile chamber slide with two wells was used for HeLa cells, with a density of 1×10^4 cells per well. The cultivated cells were treated with pure P_5W_{30} (IC_{90} = 30.87 µg/mL) and P_5W_{30}-BW-SLNs (IC_{90} = 14.72 µg/mL) for a duration of 24 hr. The cells were subjected to a 0.1% solution of Triton X-100. Subsequently, the cells were subjected to staining with DAPI (10 µg/mL) and maintained in a light-restricted environment for a duration of 10 minutes. The remaining DAPI that was not absorbed was removed by rinsing with PBS many times. The fluorescent microscope (Nikon Eclipse Japan) used for observation of HeLa cells. The wavelengths that were used for the emission and excitation phases were, respectively, 461 nm and 358 nm.[30]

Genotoxicity Assessment (Comet Assay)

The comet test, a well utilized technique for evaluating genotoxicity, was employed to quantify the level of double-strand DNA (dsDNA) damage.[30,31] HeLa cells (1×10^4 cells/well) were treated with pure P_5W_{30} (IC_{90} = 30.87 µg/mL) and P_5W_{30}-BW-SLNs (IC_{90} = 14.72 µg/mL) for a duration of 24 hr. Before being put onto comet slides, the cultivated cells were treated with 1% LMPA. To dissolve the cells, the slides were submerged in a pH-10 lysis solution. The lysis solution included 0.1% v/v Triton-X 100, 2% v/v DMSO, 10 mm Trizma X, and 100 mm EDTA. In the time-course

investigation, samples and a buffer solution containing 1 mm EDTA and 300 mm NaOH at a pH of 13 were placed in horizontally oriented electrophoretic-agarose chambers. An alkaline buffer was used to unwind the DNA. We allowed the slides to dry completely after rinsing them with methanol. The comet DNA was examined using CaspLab 1.2.3b2 software.

The Analysis of Flow Cytometry

The HeLa cell line (1×10^4) underwent to a 24-hour exposure with pure P_5W_{30} (IC_{90} = 30.87 µg/mL) and P_5W_{30}-BW-SLNs (IC_{90} = 14.72 µg/mL). The cells underwent trypsinization for 5 min at a temperature of 37 °C, using a mixture of trypsin and EDTA. To reduce the incidence of cell groupings the cell medium for cultivation was gradually introduced. The cells were collected in a binding solution (100 µL) for 15 minutes after exposure to a 500 mm concentration of H_2O_2. A fluorescent marker called annexin-V FITC with propidium iodide (PI) was used throughout this incubation. For fluorescence-triggered sorting of cells (FACS), a suitable FL2-A channel was used. The emission frequency of propidium iodide (PI) was 600 nm and that of annexin-V FITC was 545 nm. The CytoFLEX equipment (Beckman-Coulter Life Sciences, CA, USA) was used to evaluate 10,000 harvested cells in a single cycle. The data were presented using a cell cycle grading plot.[32]

Animal Studies

The study used adult female albino BALB/C mice with an average weight of 30 g. The mice were housed in the animal facility located at Bahauddin Zakariya University (60800), Multan-Pakistan. The mice were raised in a controlled setting with a constant temperature of 25°C ± 3°C. They were subjected to a light-dark cycle of 12 hr and were given unrestricted access to both food and water. A steel-mesh cage provided enough space for five albino female mice, alleviating their anxieties about crowding. Following the recommendations of the institution's ethical committee (256/PEC/2023), the animals were housed and cared for humanely. Each of the four groups consisted of five mice selected at random. Female mice were injected with HeLa cells (1×10^4) intraperitoneally (i.p). Ten days were allotted for the tumor to achieve a volume of 50–100 mm^3. The volume of a tumor in mice may be estimated without causing damage or intrusion by using calipers to measure the exterior dimensions of the tumor. This technique entails the measurement of the tumor's length (L) and width (W), followed using a formula to approximate its volume. The formula that is most often used is:[22,33,34]

$$\text{Tumor volume} = L\times W^2/2$$

The various mice groups and the therapies they received are listed in Table 2.

Each formulation's efficacy against cancer was evaluated using the tumor inhibition rate (TIR).

$$\text{TIR\%} = \left[\frac{\text{Mass of tumor in the sample group}}{\text{Tumor mass in the control group}}\right] \times 100$$

Table 2 Control and Experimental Animals Given Pure P_5W_{30}, P_5W_{30}-BW-SLNs, and Cisplatin

Group	Type of Treatment
I	Mice afflicted with cancer without treatment
2*	Mice afflicted with cancer were administered BW-SLNs
3*	Mice afflicted with cancer were administered 30 µg/kg cisplatin
4*	Mice afflicted with cancer were administered Pure P_5W_{30} (30.87 µg/kg)
5*	Mice afflicted with cancer were administered P_5W_{30}-BW-SLNs (14.72 µg/kg)

Notes: *The test compounds were administered to groups 2–5 as a single i.p dose throughout the trial.

In silico Method

Structures Preparation and Docking Studies

Sybyl-X1.3/SKETCH[35] was used to create a three-dimensional conformation of POM $((NH_4)_{14}[NaP_5W_{30}O_{110}]\cdot31H_2O)$. To get biologically active conformation, the built POM was subjected to energy optimization using the Tripos force field with Gasteiger Hückel atomic charges.[36] The co-crystal structures of Cyclin-Dependent Kinase 2 (CDK2), Protein Kinase B alpha (PKB-α), and Epidermal Growth Factor Receptor (EGFR) were retrieved from the RCSB Protein Data Bank using the corresponding PDB entries: 2FVD,[37] 4GV1,[38] and 1XKK,[39] respectively). The protein structures were subsequently subjected to processing through the structure preparation tools integrated into the SYBYL-X 1.3 biopolymer module.[40] Energy minimization was performed utilizing the Powell algorithm, with a convergence gradient set at 0.5 kcal $(mol)^{-1}$ over 1000 cycles. This process included the addition of missing hydrogens, application of charges, and assignment of atom types based on the AMBER 7 FF99 force field.[41] Lastly, using the Surflex-Dock module of the SYBYL-X 1.3 software package, the energy optimized bioactive conformation of POM was docked in to the active site of CDK2, PKB-α, and EGFR proteins using the same procedure and parameters as those described in our previous work.[42,43] The top twenty docked conformations were saved and investigated for their binding modes into the active site of their respective target. The Hammerhead scoring method was used to rate these potential ligand poses.[35,44]

Statistical Analysis

The cell cycle analysis and genotoxicity findings were subjected to statistical analysis using a paired t-test and one-way ANOVA with a significance level set at $p<0.05$. GraphPad Software's Prism 5.0 was used for the purpose of graphical depiction, whereas SPSS 9.0 (SPSS Inc. Chicago, IL, USA) was employed for statistical analysis. The findings were presented in the form of the mean standard deviation (SD).

Results and Discussion

Physical Characterization and Optimization of P_5W_{30}-BW-SLNs

Effect of Varying Surfactant Concentration

The experiment's findings demonstrated that modifying the concentration of SL and Tween 80 had a notable impact on the creation of microemulsion. Table 3 demonstrates that the creation of microemulsion was unsuccessful in cases where a surfactant combination was not used (F1-P_5W_{30}-BW-SLNs and F3-P_5W_{30}-BW-SLNs). The microemulsion was formed when a 1:1 combination of surfactant was used (F2-P_5W_{30}-BW-SLNs). *The F2-P5W30-BW-SLNs had henceforth denoted as P5W30-BW-SLNs*.

FTIR Spectroscopy

As can be seen in Figure 1A, the spectrum that was acquired by FTIR analysis includes P_5W_{30}, P_5W_{30}-BW-SLNs, and BW. In the pure P_5W_{30} spectra, a large and medium O–H stretching band was seen at a wavenumber of 3373.24 cm–1.

Table 3 Physical Characterization of Hybrid Nanoparticles

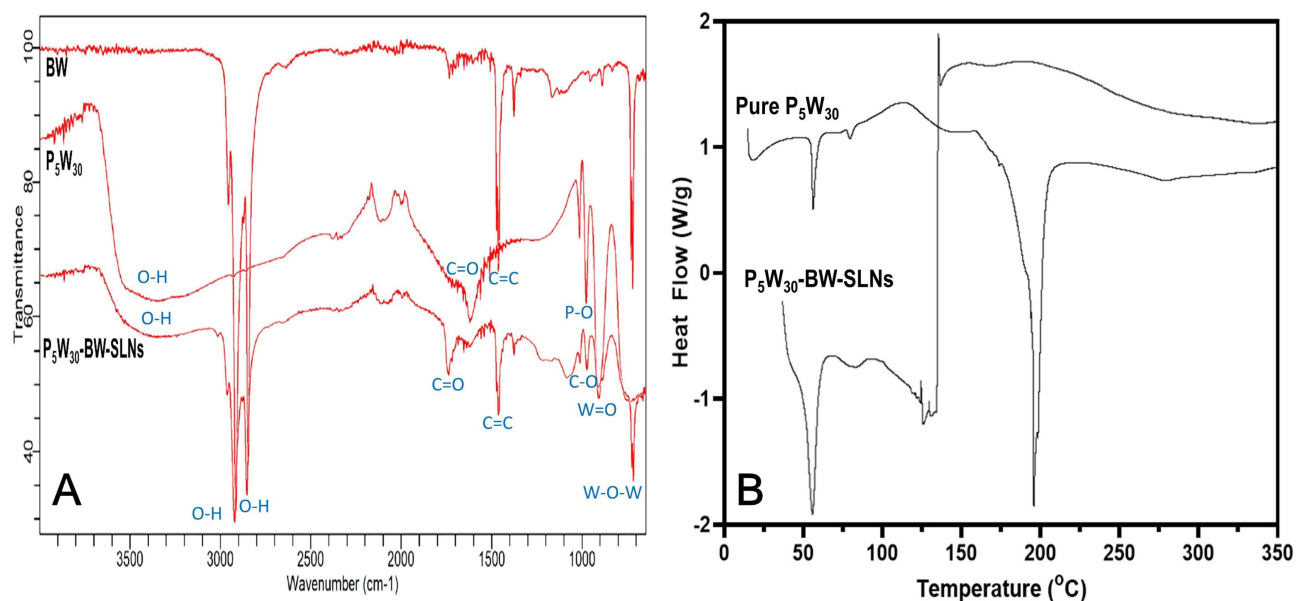| P_5W_{30}-BW-SLNs Characterization	Findings
Hydrodynamic diameter	160.5 ± 8.61 nm
Entrapment efficiency (%)	88.55 ± 4.27 (%)
Loading efficiency (%)	20.74 ± 6.39 (%)
PDI	0.3814 ± 0.096
Zeta potential (mV)	−32.57 ± 6.44 mV
Zero-order	0.9862
First-order	0.8949
Higuchi model	0.8204
Korsmeyer peppas model	0.9876
n value	1.083
IC_{50} (µg/mL) (SRB assay) Pure P_5W_{30}	7.93 ± 5.08
IC_{50} (µg/mL) (SRB assay) P_5W_{30}-BW-SLNs	3.02 ± 2.14

Figure 1 FTIR spectra of pure P_5W_{30}, BW, P_5W_{30}-BW-SLNs (**A**), DSC, Pure P_5W_{30}, P_5W_{30}-BW-SLNs (**B**).

The spectrum of P_5W_{30}-BW-SLNs showed a medium, broad and large peak (3380.69 cm^{-1}) because of O-H stretching. The FTIR spectra of BW showed one intense and large peak at 2955.77 cm^{-1} and other peaks at 2847.68 cm^{-1} due to stretching of O-H. Pure P_5W_{30} spectrum represented intensified peaks at 1684.75 cm^{-1} because of C=O stretch while that of P_5W_{30}-BW-SLNs showed clear peak at 1735.07 cm^{-1} owing to C=O stretch.[45] Intense peak was observed in BW spectra at 1462.98 cm^{-1} owing to C=C stretch. An intense peak was also found in spectra of P_5W_{30}-BW-SLNs in finger print region at 1084.65 cm^{-1} which was due to C-O stretching movements while another peak with sharp edges was at 728.69 cm^{-1} which may be because of bending vibrations. Pure P_5W_{30} showed peak of 1013.83 cm^{-1} because of P-O stretch. Another peak was shown at 907.60 cm^{-1} in region of fingerprint due to bending type vibrations at W=O. Very strong and broad W-O-W stretch pattern at 732.42 cm^{-1} was observed.[46] BW showed C-O stretch in fingerprint region at 1377.25cm^{-1} and an intense peak was also noticed at 659.73 cm^{-1} because of bending vibrations.

Differential Scanning Calorimetry (DSC) Analysis

DSC provides data on drug temperature behavior, structural changes, crystallinity, and excipient interactions.[47] The physical characteristics of a polymer can be characterized using differential scanning calorimetry. Measurement of melting points and crystallization temperatures, enthalpy and entropy changes carried out by using DSC. This technique can also be used to characterize the glass transition and other phenomena that indicate either a transition in heating capability and latent thermal heat energy.[48] In DSC thermogram (Figure 1B), the P_5W_{30} thermogram presented two endothermic shifts. There were several high points, including the glass transition temperature (Tg = 35 °C) and melting temperature (Tm =70 °C). Material showed glass transition peak at 40 °C and melting point peak at 75 °C. As the temperature rises, material starts to decompose at 165 °C.[49] A sharp peak was observed showing decomposition at 190 °C.[50] When P_5W_{30} was loaded into SLNs, two endothermic shifts were seen on DSC thermogram. It was examined that the glass transition point starts at 40 °C while its sharp peak was observed at 60 °C. The distinctive peak reflecting the melting point of the substance had vanished, suggesting the transition of pure P_5W_{30} from its crystal state to amorphous form. However, the material starts to melt at 120 °C. After that no decomposition occurs because of incorporation of P_5W_{30} into solid lipid nanoparticles which implies stability of the lipid nanocarriers system and its ability to withstand high temperature. It also suggests better holding capacity and suitability of SLNs for P_5W_{30}. Both the scans show glass transition temperature below 50 °C. The material when heated above temperature of glass transition had released the stress that have been generated in the material. At transition temperature (Tg), the structure of the molecule changes from being rigid to flexible. The material underwent a transition from a crystalline state to an amorphous state.

Percent Entrapment and Loading Efficiency

As shown in Table 3, the synthesized P_5W_{30}-BW-SLNs had remarkable entrapment and loading efficiency, with values of around $88.55 \pm 4.27\%$ and $20.74 \pm 6.39\%$ respectively. The data suggested that the SLN formulation was capable of encapsulating P_5W_{30} in an efficient manner. The effectiveness of entrapment inside SLN is highly reliant on the intrinsic properties of the drug as well as the nature of the link between the medication and the SLN components involved.[51] While simultaneously increasing the water solubility of the contained ingredient, SLNs made from BW-SL and Tween 80 were able to protect the constituent from environmental risks. Prior research has verified the notable capacity of BW-SLNs to encapsulate diverse active compounds. The experiments demonstrated that the nanocarrier had a much higher rate of optimal encapsulation.[21,52–54] The enhanced entrapment efficacy of P_5W_{30} incorporated BW-SLNs aligns with the findings obtained from our research.

Hydrodynamic Dimension and Zeta Potential Measurement

When determining particle sizes, this is crucial to consider two main factors. The first need is that particles must have a size large enough to hinder their excretion via the kidneys.[55] The second condition is that the particles have a small size to avoid being engulfed by phagocytosis and then eliminated by the system of reticuloendothelial cells (RES).[56] Current research suggests that biomolecules weighing more than 40 kDa, together with nanostructures varying in dimension from 10 to 500 nm, may pass through the network of capillaries and concentrate in the interstitial region of tumors. This process aids in the passive targeting of these substances.[57] The human body is more effective at removing particles larger than 200 nm.[58] A satisfactory hydrodynamic dimension of about 160.5 ± 8.61 nm and an appropriate polydispersity index (PDI) of 0.3814 ± 0.096 were shown by the findings of the dynamic light scattering (DLS) experiment, as shown in Figure 2A. Nanomedicines' size is crucial because it affects how well their nano-formulation mimics bioactive
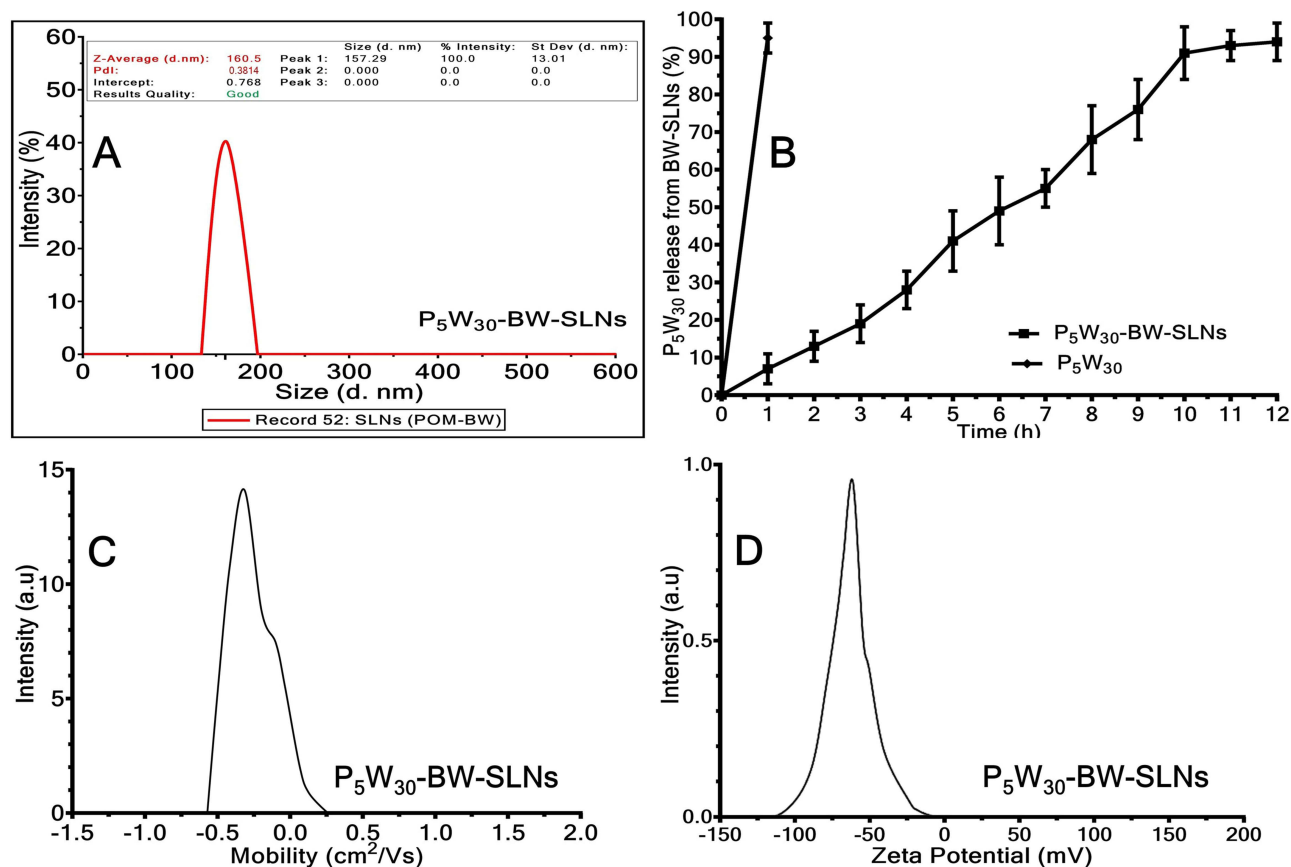

Figure 2 The physiochemical characterization of P_5W_{30}-BW-SLNs was examined by two methods: Measurement of the hydrodynamic diameter of the P_5W_{30}-BW-SLNs (**A**) and dissolution profile of P_5W_{30}-BW-SLNs at a pH of 7.4 (**B**). The data represents a particle size distribution. The peak of the curve is around -0.32 cm^2/Vs which indicates the average mobility (**C**). Zeta potential measurement of P5W30-BW-SLNs. This measurement indicates a strong negative surface charge, suggesting a high degree of stability for the SLNs (**D**).

substances, which in turn affects how well they provide therapeutic effects.[59] The hydrodynamic dimension, which measures the dispersion, biological absorption, and robustness of nanoparticles in water-based environments.[60]

The charge, stability, and dispersion capacity of P_5W_{30}-BW-SLNs were evaluated using the measurement of the zeta potential, that served as an indication of their stability. The tendency for colloidal dispersion to join and form bigger aggregates is indicated by lower zeta potential values, while higher values imply better equilibrium within the system.[61–63] The zeta potential measurements of P_5W_{30}-BW-SLNs show a negative zeta potential of between −0.6 mV (C) and −60 mV (Figure 2C and 2D). These results show that the surface of the P_5W_{30}-BW-SLNs has a net negative charge. This negative zeta potential is most likely due to the presence of negatively charged functional groups on the surface of solid lipid nanoparticles (SLNs), such as carboxyl (-COOH) and phosphate (-PO$_4$) groups. The presence of these charges promotes interactions with the surrounding media, resulting in the creation of a hydration layer around the SLNs. This hydration layer is critical for stabilizing the SLNs and preventing aggregations.

Table 3 displays the zeta potential of −32.57 ± 6.44 mV, suggesting a negative charge on the particles. The probable cause of this is the presence of the anionic surfactant Tween 80. The presence of negative charge on the SLNs may contribute to the prevention of aggregation and enhancement of their stability in solution. Beeswax is a substance that lacks polarity, while Tween 80 is a surfactant that has polarity. When used in the microemulsion technique, it is probable that the Tween 80 molecules will envelop the beeswax particles, resulting in the formation of a hydrophilic layer. A negative zeta potential often signifies a high level of electrostatic repulsion among the particles. This repulsion serves to inhibit the aggregation of particles, which is crucial for maintaining the stability and efficacy of the SLNs.[64]

Drug Kinetics and Release

The dissolution profiles presented in Figure 2B provided a visual representation of pure P_5W_{30} and P_5W_{30}-BW-SLN particles. After a period of one hour, the medium showed that pure P_5W_{30} had completely dissolved in it. Because of the low quantity of data points, it was not possible to create a kinetic model. The rapid degradation of P_5W_{30} might likely be ascribed to its very little biological half-life, that has been approximated to be less than one hour.[65] Nevertheless, the release kinetics approach was used to get a more thorough comprehension of the drug delivery system of P_5W_{30}-BW-SLNs. The investigation primarily aimed to analyze the release characteristics by using several kinetic models, such as the zero-order, first order, Peppas, and Higuchi equation. The R^2 coefficient served as a quantitative measure to assess the kinematics and release characteristics of P_5W_{30} from BW-SLNs.[66]

Table 3 had presented the R^2 data obtained from zero-order (0.9862) analysis, suggesting that the concentration of the medication does not have an impact on its release at a certain time. This study's kinetic model showed controlled drug release from SLNs. The Korsmeyer-Peppas R^2 value (0.9876, n = 1.083) demonstrated that the release of P_5W_{30} from hybrid nanosponges occurred by a non-fickian super case II type erosion and expansion mechanism. Complex polymeric systems that include the dispersion or dissolution of drugs inside a polymer matrix, or the chemical bonding of drugs to the polymer, often demonstrate non-Fickian super-case II release. The release process is influenced by several factors, including polymer erosion, expansion, relaxation, and drug dissolution or dispersion within the polymer matrix.[67]

Transmission Electron Microscopic Assessment

The surface characteristics of P5W30-BW-SLNs were assessed using transmission electron microscopy (TEM). Figure 3A demonstrates the nanoparticles' spherical form and their smooth, unbroken borders, as seen in respect to a reference scale line measuring 200 nm. The results of our investigation are consistent with previous research that has investigated the surface characteristics of SLNs.[68,69]

SEM Analysis

Utilizing scanning electron microscopy (SEM), the examination of solid lipid nanoparticles (SLNs) derived from beeswax and soy lecithin offers significant understanding of the structure and surface properties of these nanoparticles.[70] The scanning electron microscopy (SEM) pictures provide a detailed representation of the unique characteristics of the solid lipid nanoparticles (SLNs), displaying their precise dimensions, morphology, and surface structure Figure 3B. Beeswax, which acts as a lipid matrix, and soy lecithin, which contributes to the amphiphilic nature of the nanoparticles, have important functions in influencing the observed structural characteristics using SEM.
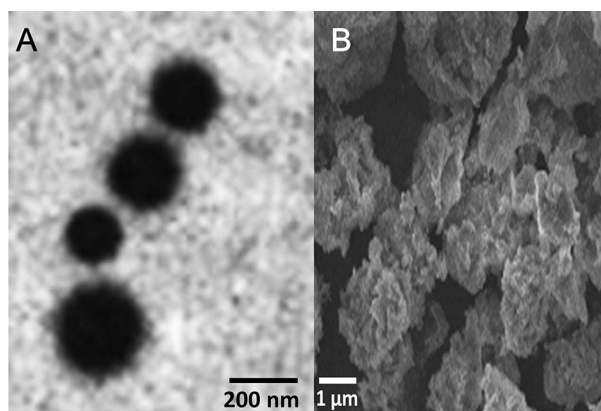
Figure 3 The representation of transmission electron microscopy image (**A**), and scanning electron microscopy image (**B**) of P_5W_{30}-BW-SLNs.

Pharmacological Assessment
Cytotoxicity and Cell Viability Assays

The SRB test was used to assess the cytotoxic effects of pure P_5W_{30} and P_5W_{30}-BW-SLNs on HeLa cells. The results of this evaluation were shown in Figure 4A. Over the course of 24 h, HeLa cells were subjected to varying concentrations of pure P_5W_{30} and P_5W_{30}-BW-SLNs. According to the data shown in Table 3, the IC_{50} values for pure P_5W_{30} and P_5W_{30}-BW-SLNs were found to be 7.93 ± 5.08 and 3.02 ± 2.14 (µg/mL), respectively. The anticancer properties of pure P_5W_{30} were investigated in a prior study, which used a more than one cancer cell lines, namely MCF-7 and HeLa cells, to determine the anticancer properties of the compound in both its pure form and when it was incorporated into nanoparticles.[71–73] The P_5W_{30}-BW-SLNs were much more effective than pure P_5W_{30} in inducing cytotoxic activity might be due to enhanced solubility and stability as compared to the unbound molecule. This may lead to increased medication concentrations at the specific location of interest (cancer cells) and enhance the efficacy of cell destruction. Furthermore, cancer cells have a higher degree of uptake efficiency for nanoparticles in comparison to unbound medicines. This is mostly attributed to the nanoparticle's dimensions and surface properties, which may enhance the cancer cell membranes contact. Finally, nanoparticles may be designed to selectively gather in tumor tissues because of the increased permeability and retention (EPR) effect. Consequently, the SLNs could efficiently transport P_5W_{30} to cancerous cells while reducing the exposure to healthy cells.[74–76]

The SRB assay measures the rate at which cells proliferate and, alternatively, the reduction in viable cells caused by metabolic processes that initiate necrosis or apoptosis.[77] The investigation shown in Figure 4B demonstrated a significant
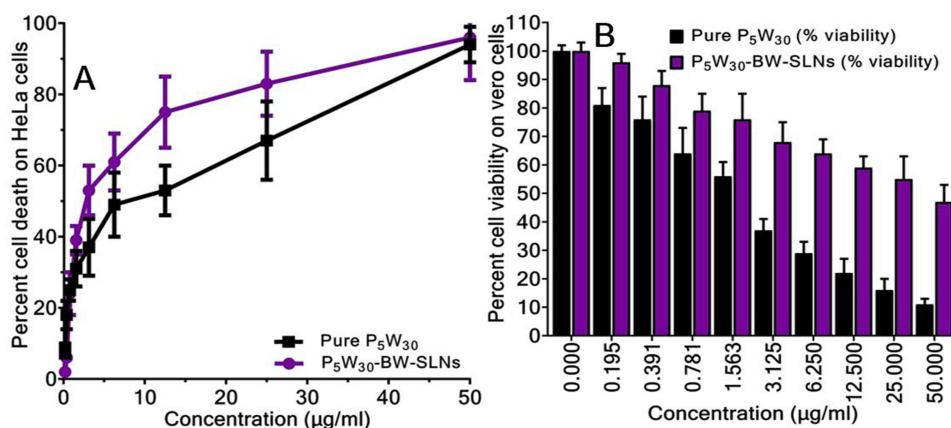

Figure 4 The pharmacological characterization assesses the proportion of HeLa and Vero cells that undergo cell death (**A**) and viability (**B**), respectively, when treated with purified P_5W_{30} and P_5W_{30}-BW-SLNs.

decrease in the viability of Vero cells, which was directly proportional to the quantity of the substance (ranging from 0 to 50 µg/mL). It is possible that the quick solubility of pure P_5W_{30} might facilitate its absorption into the tight connections of healthy cells, which would bring about a reduction in the viability of the cells. While the P_5W_{30}-BW-SLNs released pure P_5W_{30} in a regulated way, which is the reason why the nano-formulation was able to provide greater cell viability.

DAPI Staining

We utilized a qualitative test to get an understanding of the process by which POMs cause cell death. Upon treatment with P_5W_{30} cells, the HeLA cells exhibited condensed nuclei and collapsed spherical cells, as seen in Figure 5A. The presence of apoptotic bodies inside Figure 5B confirmed the process of cell death when P_5W_{30} was encapsulated within BW-SLNs. The findings of our study were consistent with those of earlier research.[71]

Genotoxicity Analysis

Utilizing the comet test allowed for the confirmation of the existence of DNA damage. Quantifying tail DNA as a fraction of total DNA content is a crucial technique used to verify the existence of DNA damage. Other strategies that were utilized include TM and OTM. The terminal segment of the genetic material (DNA) molecule had responsible for the detection of DNA damage. The experiment utilized pure P_5W_{30}, P_5W_{30}-BW-SLNs and H_2O_2 as seen in Figure 6A–6C respectively.

The estimation of DNA damage might be accomplished by assessing the difference in content of DNA among the head and tail of the comet. Table 4 demonstrated that the use of P_5W_{30}-BW-SLNs resulted in a significant rise in
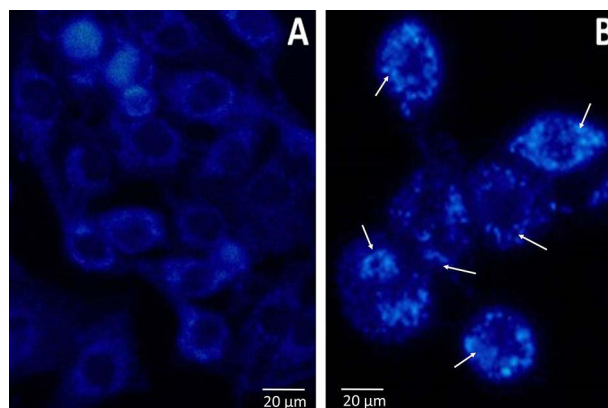

Figure 5 Representation of apoptotic cell death through DAPI staining: Pure P_5W_{30} (**A**) and P_5W_{30}-BW-SLNs (**B**). The arrows (white color) indicate apoptotic bodies in HeLa cells.
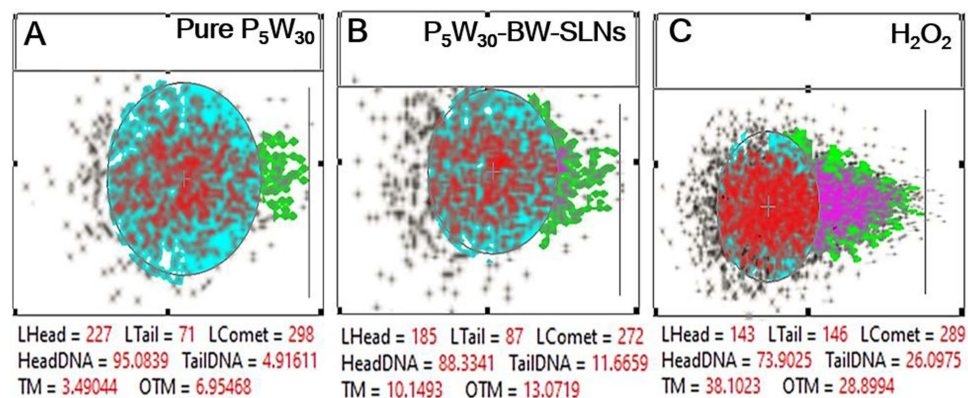

Figure 6 The comet assay demonstrates the DNA damage in HeLa cells exposed to purified P_5W_{30} (**A**), P_5W_{30}-BW-SLNs (**B**), and H_2O_2 (**C**).

Table 4 An Examination of Various Aspects Pertaining to the Comet Assay on the HeLa Cell Line Utilizing Purified P_5W_{30} and P_5W_{30}-BW-SLNs

Parameters of Comet Assay	Pure P_5W_{30}	P_5W_{30}-BW-SLNs	H_2O_2
L-Head	227	185	143
L-Tail	71	87	146
L-Comet	298	272	289
Head-DNA	95.08	88.33	73.90
Tail-DNA	4.91	11.66	26.09
TM	3.49	10.14	38.10
OTM	6.95	13.07	28.89

damaged DNA of HeLa cells, in comparison to the usage of pure P_5W_{30}. The quantification of DNA damage may be accomplished by analyzing the disparity in the amount of DNA between the head and tail parts of the comet.[33,34]

The Analysis of Flow Cytometry

The flow cytometry method was used to get more understanding of the phases of cell cycle arrest, mitochondrial function and apoptosis.[78]

The flow cytometry experiment confirmed the quantitative aspect of the previously subjective findings on cancer cell death. Figure 7A shows that in the absence of medication (control group), a higher proportion of HeLa cells ($86.2 \pm 3.19\%$) remained in the G0/G1 phase, whereas only a tiny fraction of cells was observed in the sub-G1 phase ($0.17 \pm 0.045\%$). The cells demonstrated an elevated rate of cellular apoptosis when exposed to pure P_5W_{30}, as shown by an augmentation in sub-G1 ($4.97 \pm 1.72\%$) levels and a subsequent reduction in the proportion of cells during the G0/G1 ($77.4 \pm 5.38\%$) phase, illustrated in Figure 7B histograms. The exposure concerning HeLa cells with P_5W_{30}-BW-SLNs resulted in increased cell death, as shown by a greater percentage of sub-G1 cells ($11.6 \pm 3.04\%$) with a lower proportion of G0/G1 cells ($65.7 \pm 5.89\%$) (Figure 7C). Figure 7D displayed the distribution of cells in different stages of the cell cycle after being treated with P_5W_{30}-BW-SLNs, pure P_5W_{30}, or a control. The current research's findings corroborated those of a previous study that found that hydrolysates of fenugreek protein inhibited the proliferation of colorectal cancer cells. The hydrolysates have shown the ability to impede cell proliferation by augmenting intrinsic apoptosis.[79]

Animal Studies

For validating the data gained through in vitro experiments, the study used female albino mice as respondents in an in vivo study. Figure 8A and Table 5 displayed the survival rates of mice that were fed various dosages of cisplatin
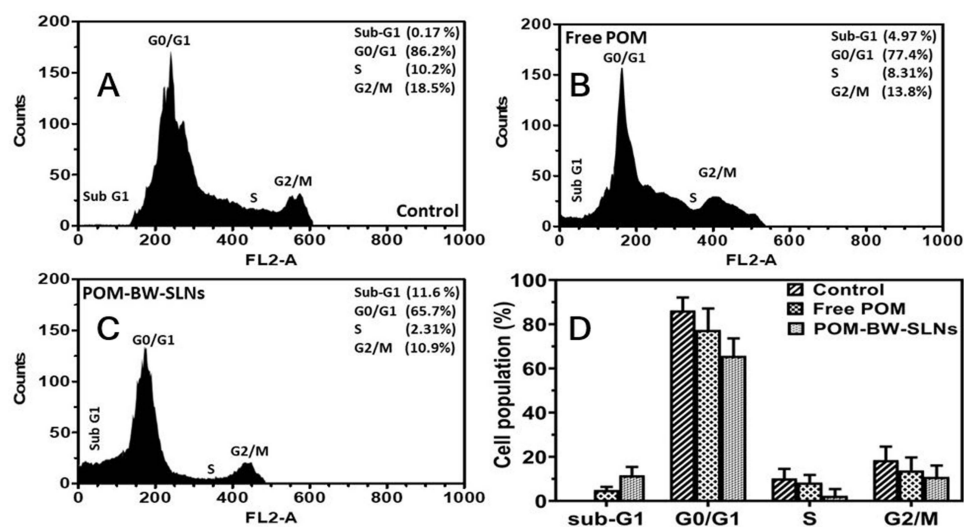

Figure 7 Flow cytometry analysis of HeLa cells treated with control (**A**), pure P5W30 (**B**), and P_5W_{30}-BW-SLNs (**C**). The percentage of cells treated throughout the cell cycle (**D**) with pure P_5W_{30}, P_5W_{30}-BW-SLNs, or a control. (Results show a significant difference ($p<0.05$).
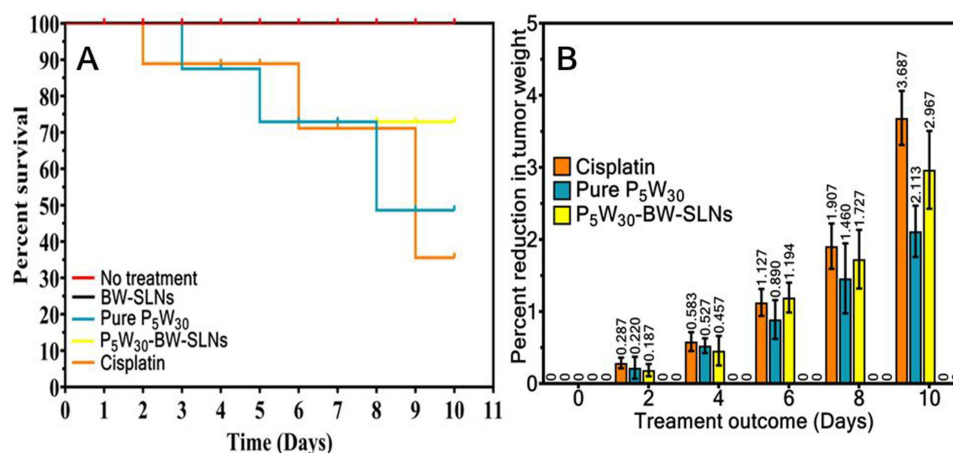
Figure 8 The in vivo longevity rate (**A**) and the % reduction in tumor weight (**B**) of pure P_5W_{30}, and P_5W_{30}-BW-SLNs treated with HeLa cells. Statistical significance was determined using ANOVA, with a p-value of <0.05 indicating significant differences between the treatment groups.

(30 μg/kg), pure P_5W_{30} (30.87 μg/kg), and P_5W_{30}-BW-SLNs (14.72 μg/kg). A comparison was made between the findings and the standard that had been set for cisplatin effectiveness. When compared to the group that was treated alone with pure P_5W_{30} plus the conventional anticancer medication cisplatin, the group that was given P_5W_{30}-BW-SLNs showed a higher survival rate.[80]

The present research included the analysis of the percentage of malignant mice that survived under various treatment conditions over a period of 10 days. The treatments consisted of Cisplatin, Pure P_5W_{30}, P_5W_{30}-BW-SLNs, BW-SLNs, and a control group that did not receive any therapy. On the first day of the trial (Day 0), all groups showed complete survival. During the following days, the group that received Cisplatin treatment had a complete survival rate. However, on Day 2, there was a decline to 88.89% which continued until Day 5. On the other hand, the Pure P_5W_{30} group showed complete survival until Day 8, but then had a decrease to 48.61% on Day 10. The P_5W_{30}-BW-SLNs administered group exhibited 87.5% survival rate until Day 4, after which a progressive decrease was observed, reaching 72.91% on Day 10. Significantly, Group 1 and Group 2 demonstrated 100% survival over the whole duration of the investigation. The findings indicated that P_5W_{30}-BW-SLNs had a positive impact on prolonging life as compared to P_5W_{30} and cisplatin (survival percent at day-10th 48.61 and 35.56 respectively) (p<0.05). These results emphasize the possible influence of various therapies on the survival rates of mice with cancer and justify the need for more research on the mechanisms and efficacy of each therapeutic option in this experimental setting.

In Figure 8B, the group that received P_5W_{30}-BW-SLNs therapy observed a more significant reduction in tumor weight % compared to the group which obtained pure P_5W_{30} alone, on the 10th day after administration. It has been

Table 5 Percent Survival Data of Cancerous Mice

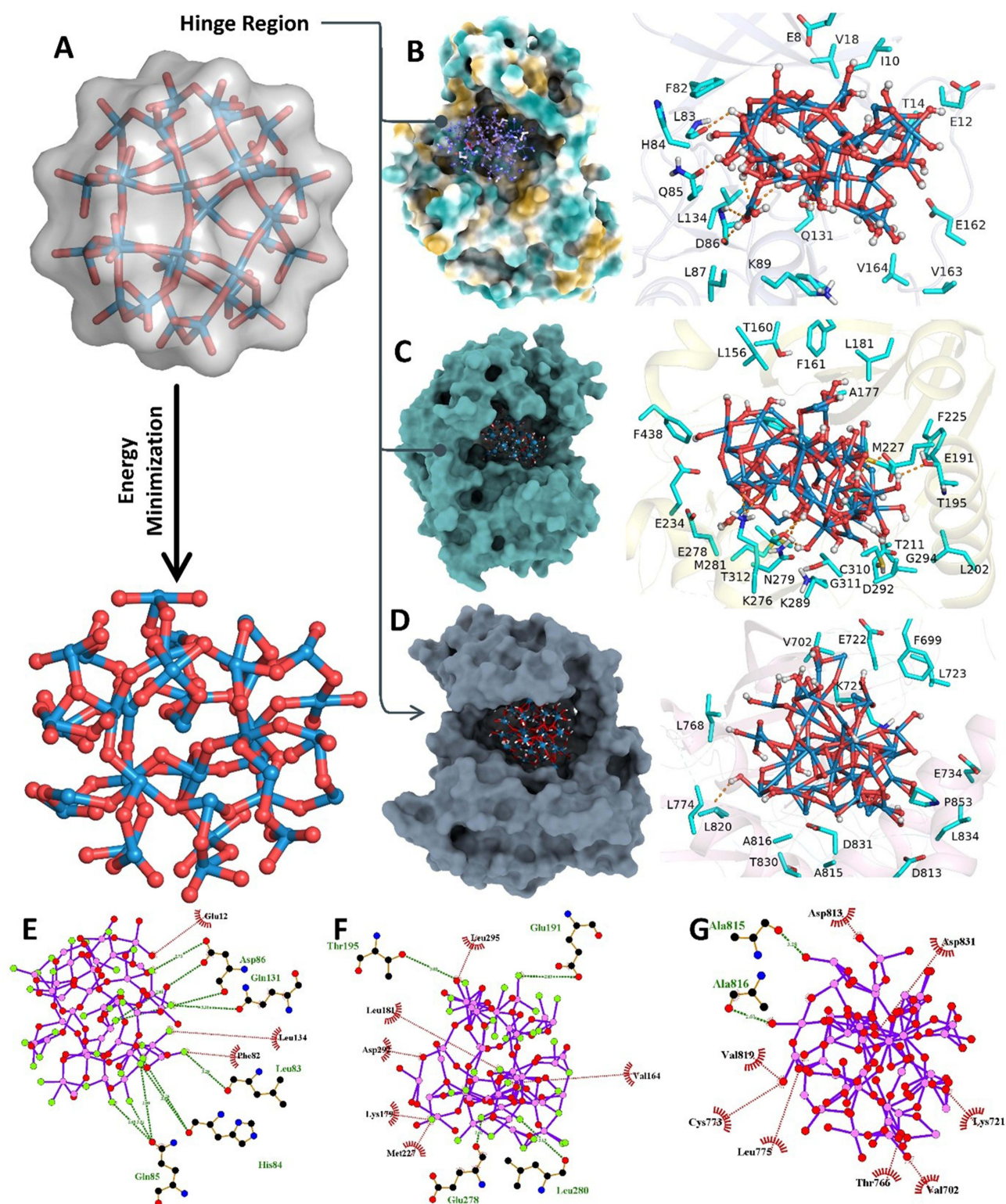| Days	Cisplatin	Pure P_5W_{30}	P_5W_{30}-BW-SLNs	BW-SLNs	No Treatment
0	100	100	100	100	100
1	100	100	100	100	100
2	88.89	100	100	100	100
3	88.89	87.5	87.5	100	100
4	88.89	87.5	87.5	100	100
5	88.89	72.91	72.91	100	100
6	71.11	72.91	72.91	100	100
7	71.11	72.91	72.91	100	100
8	71.11	48.61	72.91	100	100
9	35.56	48.61	72.91	100	100
10	35.56	48.61	72.91	100	100

Figure 9 Docking generated complexes of POM bonded to its corresponding molecular target CDK2 (hydrophobic, light blue), PCG (green, yellow) and EGFR (slate, purple): (**A** and **E**) CDK2-POM, (**C** and **F**) POM-PKB-α, (**D** and **G**) EGFR-POM. H-bonds are displayed in Orange dotted lines.

found that cisplatin is a chemotherapeutic drug that is often employed. This substance is known to interrupt the process of DNA replication in cells that are quickly growing, such as cancer cells. This was evidenced by the considerable $3.687 \pm 0.375\%$ reduction in tumor weight, which proved its efficiency in inhibiting the formation of tumors. The administration of P_5W_{30} resulted in a reduction of $2.113 \pm 0.402\%$ in the weight of the tumor, which indicates that it had

Table 6 Surflex Scores of Docked Ligand POM in the Binding Site of Proteins CDK2, PKB-α and EGFR

Inhibitor	Docking Complex	CScore[a]	Crash Score[b]	Polar Score[c]	D Score[d]	PMF Score[e]	G Score[f]	Chem Score[g]
POM	CDK2	**68.21**	−11.44	46.34	−3277.41	−103.56	−947.38	−32.50
	PKB-α	**47.93**	−6.13	30.83	−1522.17	−97.02	−643.68	−18.53
	EGFR	44.15	−4.55	32.13	−1027.53	−67.45	−264.14	−15.98

Notes: [a]**CScore** is a consensus scoring which uses multiple types of scoring functions to rank the affinity of ligands, [b]**Crash**-score revealing the inappropriate penetration into the binding site, [c] **Polar** region of the ligand, [d] **D**-score showing hydrogen bonding, complex (ligand-protein), and internal (ligand-ligand) energies, [e] **PMF**-score indicating the Helmholtz free energies of interactions for protein-ligand atom pairs (Potential of Mean Force, PMF), [f] **G**-score for charge and van der Waals interactions between the protein and the ligand, [g] **Chem**-score points for hydrogen bonding, lipophilic contact, and rotational entropy, along with an intercept term.

a moderate influence on suppressing the development of the tumor in comparison to cisplatin, which generated a decrease of 3.687 ± 0.375%. The tumor weight reduction of 2.967 ± 0.543% indicates that the effects of P_5W_{30}-BW-SLNs are stronger to those of purified P_5W_{30}. The potential utilization of nanoparticles to enhance the delivery and localization of therapeutic drugs to the site of the tumor could result in improved efficacy and reduced adverse effects. Prior research has shown evidence for the benefits of nanoparticles in enabling regulated and precise delivery of medications, hence improving the efficacy of therapy in different cancer treatment regimens.[81]

Molecular Docking Studies

Molecular docking is among the most employed approaches to unveil the binding mechanisms of ligands towards various molecular targets.[82–87] Utilizing an in-silico approach can yield valuable insights into the structural and functional relationships within ligand-protein systems, aiding our comprehension of the molecular mechanisms that impede the rapid growth of cancerous cell lines. Through both in-vivo and in-vitro analyses (Figure 9), a noticeable reduction in growth was observed in the HeLA cell line upon continuous exposure to POM. To gain a comprehensive understanding, an extensive literature survey was conducted to identify three pivotal proteins CDK2, PKB-α, and EGFR that regulate distinct signaling pathways in HeLA cells.[88,89] Subsequently, molecular docking was employed to unveil the mechanism underpinning the anti-proliferative potential of POM.

Leveraging the cumulative score (cScore), optimal ligand poses within protein active sites were identified. Docking scores (cScore) for inhibitor POM binding to CDK2, PKB-α, and EGFR are 68.21, 47.93, and 44.15, respectively. These scores suggest POM forms the most robust complex with CDK2, though it efficiently binds to PKB-α and EGFR. Overall, the docking scores indicate commendable binding affinity for all three proteins, with a slightly higher affinity for CDK2. Detailed docking results, including scores, are presented in Table 6. To comprehend docking score variations, top-ranked docking complexes were saved and visually examined (Figure 9A–9G). Figure 9A illustrates substantial conformational changes in inhibitor POM, adopting a complex shape post energy minimization. Despite POM's intricate structure with numerous oxygen atoms, it establishes several H-bond contacts with nearby residues in all protein-ligand complexes, supporting its higher docking scores. In the CDK2-bonded system, POM deeply penetrates the active site between N- and C-terminal domains, interacting with residues such as E8, I10, V18, E12, T14, F80, E81, F82, L83, Q85, D86, Q131, E162, and V164 (Figure 9B). Conserved H-bond interactions with L83 in the hinge region are crucial, with POM forming additional bonds with Q85 and D86 in the solvent-exposed region. hese residues have been consistently highlighted in previous publications, demonstrating their crucial role in facilitating the binding of potent CDK2 inhibitors.[42,43,90] For the PKB-bonded system, POM occupies the ligand binding cavity, but its large structure prevents reaching the hinge region. Consequently, POM establishes maximum interactions in the solvent-exposed region, forming at least six H-bonds with residues T195, M227, K276, N279, and T319 (Figure 1C). In the EGFR-bonded system, only a couple of H-bond interactions are observed. The binding cavity in the EGFR-POM bonded system includes V702, K721, T766, C773, L775, D813, A815, D831, and A816. Similar to the POM-PKB complex, in the EGFR-inhibitor complex, POM remains near the solvent-exposed region and does not exploit hinge residues. For more better under-standing the 2D interaction diagram of inhibitor-protein complex is displayed in Figure 9E–9G In conclusion, these findings explain the enhanced binding affinity of POM towards CDK2. The computational results strongly correlate with

experimental findings, providing a plausible explanation for POM's substantial chemopreventive efficacy against HeLa cell lines.

Conclusion

The incorporation of polyoxometalates into solid lipid nanoparticles is a multidimensional method that has the potential to have positive consequences for the treatment of cancer. The study's physical characterization reveals these nanoparticles' structural features, revealing their stability and biological connections. Pharmacological tests show polyoxometalate-loaded nanoparticles' cancer therapy effectiveness and therapeutic potential. Computational studies help anticipate molecular interactions and optimize nanoparticle design for anticancer effects. The findings demonstrate polyoxometalate-integrated solid lipid nanoparticles' potential as a multifunctional cancer therapy platform, bridging chemistry, pharmacology, and computational sciences to develop novel and effective treatments.

Institutional Review Board (IRB) Statement

The research committee on Biosafety and Bioethics at Bahauddin Zakariya University Multan (60800), Pakistan, gave their stamp of approval (256/PEC/2023) to the study protocol titled. "Beyond chemistry: Investigating the physical, pharmacological and computational aspects of polyoxometalate integrated solid lipid nanoparticles for cancer treatment". The researchers have been advised to follow the ethics committee-approved protocol precisely when working with mice.

Sample Availability

The authors may provide the sample substances upon a fair request from the corresponding author.

Acknowldegments

Author Contributions

All authors made a significant contribution to the work reported, whether that is in the conception, study design, execution, acquisition of data, analysis and interpretation, or in all these areas; took part in drafting, revising or critically reviewing the article; gave final approval of the version to be published; have agreed on the journal to which the article has been submitted; and agree to be accountable for all aspects of the work.

Disclosure

The authors report no conflicts of interest in this work.

References

1. Vilà-Nadal L, Cronin L. Design and synthesis of polyoxometalate-framework materials from cluster precursors. *Nature Rev Mater*. 2017;2(10):1–15. doi:10.1038/natrevmats.2017.54
2. Čolović MB, Lacković M, Lalatović J, Mougharbel AS, Kortz U, Krstić DZ. Polyoxometalates in biomedicine: update and overview. *Curr Med Chem*. 2020;27(3):362–379. doi:10.2174/0929867326666190827153532
3. Guedes G, Wang S, Santos HA, Sousa FL. Polyoxometalate composites in cancer therapy and diagnostics. *Eur J Inorg Chem*. 2020;2020(22):2121–2132. doi:10.1002/ejic.202000066
4. Aureliano M. The future is bright for polyoxometalates. *BioChem*. 2022;2(1):8–26. doi:10.3390/biochem2010002
5. Carvalho F, Aureliano M. Polyoxometalates impact as anticancer agents. *Int J Mol Sci*. 2023;24(5):5043. doi:10.3390/ijms24055043
6. Chang D, Li Y, Chen Y, Wang X, Zang D, Liu T. Polyoxometalate-based nanocomposites for antitumor and antibacterial applications. *Nanoscale Adv*. 2022;4(18):3689. doi:10.1039/D2NA00391K
7. Bijelic A, Aureliano M, Rompel A. Polyoxometalates as potential next-generation metallodrugs in the combat against cancer. *Angew Chem Int Ed*. 2019;58(10):2980–2999. doi:10.1002/anie.201803868
8. Yue Z, Wang R, Li J, et al. Recent Advances in Polyoxometalate Based Nanoplatforms Mediated Reactive Oxygen Species Cancer Therapy. *Chemistry – an Asian Journal*. 2023;18(22):e202300749. doi:10.1002/asia.202300749
9. Pu F, Wang E, Jiang H, Ren J. Identification of polyoxometalates as inhibitors of basic fibroblast growth factor. *Mol Biosyst*. 2013;9(1):113–120. doi:10.1039/C2MB25389E

10. Wang X, Wei S, Zhao C, et al. Promising application of polyoxometalates in the treatment of cancer, infectious diseases and Alzheimer's disease. *J Biol Inorg Chem*. 2022;27(4–5):405–419. doi:10.1007/s00775-022-01942-7

11. Lu F, Wang M, Li N, Tang B. Polyoxometalate-Based Nanomaterials toward Efficient Cancer Diagnosis and Therapy. *Chemistry*. 2021;27 (21):6422–6434.

12. Long DL, Tsunashima R, Cronin L. Polyoxometalates: building blocks for functional nanoscale systems. *Angew Chem Int Ed*. 2010;49 (10):1736–1758. doi:10.1002/anie.200902483

13. Mendoza-Munoz N, Urbán-Morlán Z, Leyva-Gómez G, De la luz zambrano-zaragoza M, Quintanar-Guerrero D, Quintanar-Guerrero D. Solid lipid nanoparticles: an approach to improve oral drug delivery. *J Pharm Pharm Sci*. 2021;24:509–532. doi:10.18433/jpps31788

14. Ndagi U, Mhlongo N, Soliman ME. Metal complexes in cancer therapy – an update from drug design perspective. *Drug Des Devel Ther*. 2017; Volume11:599–616. doi:10.2147/DDDT.S119488

15. Mishra DK, Shandilya R, Mishra PK. Lipid based nanocarriers: a translational perspective. *Nanomed Nanotechnol Biol Med*. 2018;14 (7):2023–2050. doi:10.1016/j.nano.2018.05.021

16. Lim SB, Banerjee A, Önyüksel H. Improvement of drug safety by the use of lipid-based nanocarriers. *J Control Release*. 2012;163(1):34–45. doi:10.1016/j.jconrel.2012.06.002

17. Bhatt S, Sharma J, Singh M, Saini V. Solid lipid nanoparticles: a promising technology for delivery of poorly water-soluble drugs. *Acta Pharma Sci*. 2018;56(3):27. doi:10.23893/1307-2080.APS.05616

18. Chauhan I, Singh L. A Comprehensive Literature Review of Lipids Used in the Formulation of Lipid Nanoparticles. *Curr Nanomater*. 2023;8 (2):126–152. doi:10.2174/2405461507666220606164446

19. Soleimanian Y, Goli SAH, Shirvani A, Elmizadeh A, Marangoni AG. Wax-based delivery systems: preparation, characterization, and food applications. *Compr Rev Food Sci Food Saf*. 2020;19(6):2994–3030. doi:10.1111/1541-4337.12614

20. Cimino C, Maurel OM, Musumeci T, et al. Essential oils: pharmaceutical applications and encapsulation strategies into lipid-based delivery systems. *Pharmaceutics*. 2021;13(3):327. doi:10.3390/pharmaceutics13030327

21. Kheradmandnia S, Vasheghani-Farahani E, Nosrati M, Atyabi F. Preparation and characterization of ketoprofen-loaded solid lipid nanoparticles made from beeswax and carnauba wax. *Nanomed Nanotechnol Biol Med*. 2010;6(6):753–759. doi:10.1016/j.nano.2010.06.003

22. Shah HS, Usman F, Ashfaq–Khan M, et al. Preparation and characterization of anticancer niosomal withaferin–A formulation for improved delivery to cancer cells: in vitro, in vivo, and in silico evaluation. *J Drug Delivery Sci Technol*. 2020;59:101863. doi:10.1016/j.jddst.2020.101863

23. Shah HS, Khalid F, Bashir S, et al. Emulsion-templated synthesis and in vitro characterizations of niosomes for improved therapeutic potential of hydrophobic anti-cancer drug: tamoxifen. *J Nanopart Res*. 2019;21(2):1–10. doi:10.1007/s11051-019-4464-y

24. Pushpalatha R, Selvamuthukumar S, Kilimozhi D. Cross-linked, cyclodextrin-based nanosponges for curcumin delivery-Physicochemical characterization, drug release, stability and cytotoxicity. *J Drug Delivery Sci Technol*. 2018;45:45–53. doi:10.1016/j.jddst.2018.03.004

25. Varan C, Anceschi A, Sevli S, et al. Preparation and characterization of cyclodextrin nanosponges for organic toxic molecule removal. *Int J Pharm*. 2020;585:119485. doi:10.1016/j.ijpharm.2020.119485

26. Mohamed N. Synthesis of hybrid chitosan silver nanoparticles loaded with doxorubicin with promising anti-cancer activity. *BioNanoScience*. 2020;10(3):758–765. doi:10.1007/s12668-020-00760-y

27. Ul-Hamid A, Ul-Hamid A. *A Beginners' Guide to Scanning Electron Microscopy*. 2018;1 309–359.

28. Vichai V, Kirtikara K. Sulforhodamine B colorimetric assay for cytotoxicity screening. *Nat Protocols*. 2006;1(3):1112–1116. doi:10.1038/nprot.2006.179

29. Riss TL, Moravec RA, Niles AL, et al. Cell viability assays. *Assay Guidance Manual*. 2016;2016:1.

30. Priyadarsini RV, Murugan RS, Maitreyi S, Ramalingam K, Karunagaran D, Nagini S. The flavonoid quercetin induces cell cycle arrest and mitochondria-mediated apoptosis in human cervical cancer (HeLa) cells through p53 induction and NF-κB inhibition. *Eur J Pharmacol*. 2010;649 (1–3):84–91. doi:10.1016/j.ejphar.2010.09.020

31. Singh NP, McCoy MT, Tice RR, Schneider EL. A simple technique for quantitation of low levels of DNA damage in individual cells. *Exp Cell Res*. 1988;175(1):184–191. doi:10.1016/0014-4827(88)90265-0

32. Lin G-J, Jiang G-B, Xie -Y-Y, Huang H-L, Liang Z-H, Liu Y-J. Cytotoxicity, apoptosis, cell cycle arrest, reactive oxygen species, mitochondrial membrane potential, and Western blotting analysis of ruthenium (II) complexes. *J Biol Inorg Chem*. 2013;18(8):873–882. doi:10.1007/s00775-013-1032-2

33. Shah HS, Nasrullah U, Zaib S, et al. Preparation, characterization, and pharmacological investigation of withaferin-A loaded nanosponges for cancer therapy; in vitro, in vivo and molecular docking studies. *Molecules*. 2021;26(22):6990. doi:10.3390/molecules26226990

34. Shah HS, Zaib S, Sarfraz M, et al. Fabrication and Evaluation of Anticancer Potential of Eugenol Incorporated Chitosan-Silver Nanocomposites: in Vitro, In Vivo, and In Silico Studies. *AAPS Pharm Sci Tech*. 2023;24(6):168.

35. Jain AN. Surflex: fully automatic flexible molecular docking using a molecular similarity-based search engine. *J Med Chem*. 2003;46(4):499–511. doi:10.1021/jm020406h

36. Powell MJ. A fast algorithm for nonlinearly constrained optimization calculations. In: *Numerical Analysis*. Springer; 1978:144–157.

37. Chu X-J, DePinto W, Bartkovitz D, et al. Discovery of [4-amino-2-(1-methanesulfonylpiperidin-4-ylamino) pyrimidin-5-yl](2, 3-difluoro-6-methoxyphenyl) methanone (R547), a potent and selective cyclin-dependent kinase inhibitor with significant in vivo antitumor activity. *J Med Chem*. 2006;49(22):6549–6560. doi:10.1021/jm0606138

38. Addie M, Ballard P, Buttar D, et al. Discovery of 4-Amino-N-[(1 S)-1-(4-chlorophenyl)-3-hydroxypropyl]-1-(7 H-pyrrolo [2, 3-d] pyrimidin-4-yl) piperidine-4-carboxamide (AZD5363), an Orally Bioavailable, Potent Inhibitor of Akt Kinases. *J Med Chem*. 2013;56(5):2059–2073. doi:10.1021/jm301762v

39. Wood ER, Truesdale AT, McDonald OB, et al. A unique structure for epidermal growth factor receptor bound to GW572016 (Lapatinib) relationships among protein conformation, inhibitor off-rate, and receptor activity in tumor cells. *Cancer Res*. 2004;64(18):6652–6659. doi:10.1158/0008-5472.CAN-04-1168

40. Ghersi D, Sanchez R. Beyond structural genomics: computational approaches for the identification of ligand binding sites in protein structures. *J Struct Funct Genomics*. 2011;12(2):109–117. doi:10.1007/s10969-011-9110-6

41. Onufriev A, Bashford D, Case DA. Exploring protein native states and large-scale conformational changes with a modified generalized born model. *Proteins Struct Funct Bioinf*. 2004;55(2):383–394. doi:10.1002/prot.20033

42. Chohan TA, Qian H-Y, Pan Y-L, Chen J-Z. Molecular simulation studies on the binding selectivity of 2-anilino-4-(thiazol-5-yl)-pyrimidines in complexes with CDK2 and CDK7. *Mol Biosyst*. 2016;12(1):145–161. doi:10.1039/C5MB00630A

43. Chohan TA, Sarfraz M, Rehman K, et al. Phytochemical profiling, antioxidant and antiproliferation potential of Euphorbia milii var.: experimental analysis and in-silico validation. *Saudi J Biol Sci*. 2020;27(11):3025–3034. doi:10.1016/j.sjbs.2020.08.003

44. Jain AN. Scoring noncovalent protein-ligand interactions: a continuous differentiable function tuned to compute binding affinities. *J Comput Mol Des*. 1996;10(5):427–440. doi:10.1007/BF00124474

45. Carraro M, Fiorani G, Mognon L, et al. Hybrid Polyoxotungstates as Functional Comonomers in New Cross-Linked Catalytic Polymers for Sustainable Oxidation with Hydrogen Peroxide. *Chemistry (Weinheim an der Bergstrasse, Germany)*. 2012;18(41):13195–13202. doi:10.1002/chem.201201849

46. Rs B. Differentiation of mono-oxo and polyoxo and of monomeric and polymeric vanadate, molybdate and tungstate species in metal oxide catalysts by IR and Raman spectroscopy. *J Raman Spectroscopy*. 2002;33(5):348–358. doi:10.2144/02332rr01

47. Moin A, Roohi NF, Rizvi SMD, et al. Design and formulation of polymeric nanosponge tablets with enhanced solubility for combination therapy. *RSC Advances*. 2020;10(57):34869–34884. doi:10.1039/d0ra06611g

48. Schick C. Differential scanning calorimetry (DSC) of semicrystalline polymers. *Anal Bioanal Chem*. 2009;395(6):1589–1611. doi:10.1007/s00216-009-3169-y

49. López-Benítez A, Guevara-Lara A, Berhault GJAC. Nickel-containing polyoxotungstates based on [PW9O34] 9–and [PW10O39] 13–Keggin lacunary anions supported on Al2O3 for dibenzothiophene hydrodesulfurization application. *ACS Calal*. 2019;9(8):6711–6727. doi:10.1038/s41598-019-43160-3

50. Li Q, Yjcc W. A series of unprecedented triol-stabilized [H 3 MW 6 O 24] n−: the missing piece between A-and B-type Anderson–Evans polyoxometalates. *Chemical Communications (Cambridge, England)*. 2018;54(11):1375–1378. doi:10.1039/c7cc08976g

51. Liu Q, Duan B, Xu X, Zhang L. Progress in rigid polysaccharide-based nanocomposites with therapeutic functions. *J Mater Chem B*. 2017;5(29):5690–5713. doi:10.1039/C7TB01065F

52. Attama AA, Müller-Goymann CC. Effect of beeswax modification on the lipid matrix and solid lipid nanoparticle crystallinity. *Colloids Surf A*. 2008;315(1–3):189–195. doi:10.1016/j.colsurfa.2007.07.035

53. Dantas IL, Bastos KTS, Machado M, et al. Influence of stearic acid and beeswax as solid lipid matrix of lipid nanoparticles containing tacrolimus. *J Therm Anal Calorimet*. 2018;132(3):1557–1566. doi:10.1007/s10973-018-7072-7

54. Nguyen HM, Hwang IC, Park JW, Park HJ. Photoprotection for deltamethrin using chitosan-coated beeswax solid lipid nanoparticles. *Pest Manage Sci*. 2012;68(7):1062–1068. doi:10.1002/ps.3268

55. Raj S, Khurana S, Choudhari R, et al. Specific targeting cancer cells with nanoparticles and drug delivery in cancer therapy. Paper presented at: Seminars in cancer biology. 2021.

56. Betzer O, Shilo M, Opochinsky R, et al. The effect of nanoparticle size on the ability to cross the blood–brain barrier: an in vivo study. *Nanomedicine*. 2017;12(13):1533–1546. doi:10.2217/nnm-2017-0022

57. Torchilin V. Tumor delivery of macromolecular drugs based on the EPR effect. *Adv Drug Delivery Rev*. 2011;63(3):131–135. doi:10.1016/j.addr.2010.03.011

58. Parmar K, Patel J, Pathak Y. Factors Affecting the Clearance and Biodistribution of Polymeric Nanoparticles. In: *Pharmacokinetics and Pharmacodynamics of Nanoparticulate Drug Delivery Systems*. Springer; 2022:261–272.

59. Hackley VA, Clogston JD. Measuring the hydrodynamic size of nanoparticles in aqueous media using batch-mode dynamic light scattering. *Characterization of Nanoparticles Intended for Drug Delivery*. 2011;2011:35–52.

60. Chai MHH, Amir N, Yahya N, Saaid IM. Characterization and colloidal stability of surface modified zinc oxide nanoparticle. Paper presented at: Journal of Physics: Conference Series. 2018.

61. Kurpiers M, Wolf JD, Steinbring C, Zaichik S, Bernkop-Schnürch A. Zeta potential changing nanoemulsions based on phosphate moiety cleavage of a PEGylated surfactant. *J Mol Liq*. 2020;316:113868. doi:10.1016/j.molliq.2020.113868

62. Kamble S, Agrawal S, Cherumukkil S, Sharma V, Jasra RV, Munshi P. Revisiting zeta potential, the key feature of interfacial phenomena, with applications and recent advancements. *ChemistrySelect*. 2022;7(1):e202103084. doi:10.1002/slct.202103084

63. Larsson M, Hill A, Duffy J. Suspension stability; why particle size, zeta potential and rheology are important. *Annu trans Nord rheol soc*. 2012;20(2012):6.

64. Albanese A, Tang PS, Chan WC. The effect of nanoparticle size, shape, and surface chemistry on biological systems. *Ann Rev Biomed Eng*. 2012;14(1):1–16. doi:10.1146/annurev-bioeng-071811-150124

65. Long J, Guo Y, Yang J, et al. Bioavailability and bioactivity of free ellagic acid compared to pomegranate juice. *Food Funct*. 2019;10(10):6582–6588. doi:10.1039/C9FO01683J

66. Naseer F, Ahmad T, Kousar K, Kakar S, Gul R, Anjum S. Formulation of surface-functionalized hyaluronic acid-coated thiolated chitosan nano-formulation for the delivery of vincristine in prostate cancer: a multifunctional targeted drug delivery approach. *J Drug Delivery Sci Technol*. 2022;74:103545. doi:10.1016/j.jddst.2022.103545

67. Chen L, Zheng Y, Feng L, Liu Z, Guo R, Zhang Y. Novel hyaluronic acid coated hydrophobically modified chitosan polyelectrolyte complex for the delivery of doxorubicin. *Int J Biol Macromol*. 2019;126:254–261. doi:10.1016/j.ijbiomac.2018.12.215

68. Wang W, Liu M, Gao W, Sun Y, Dong X. Coassembled Chitosan–Hyaluronic Acid Nanoparticles as a Theranostic Agent Targeting Alzheimer's β-Amyloid. *ACS Appl Mater Interfaces*. 2021;13(47):55879–55889. doi:10.1021/acsami.1c17267

69. Amekyeh H, Billa N. Lyophilized drug-loaded solid lipid nanoparticles formulated with beeswax and theobroma oil. *Molecules*. 2021;26(4):908. doi:10.3390/molecules26040908

70. Gordillo-Galeano A, Mora-Huertas CE. Solid lipid nanoparticles and nanostructured lipid carriers: a review emphasizing on particle structure and drug release. *Eur J Pharm Biopharm*. 2018;133:285–308. doi:10.1016/j.ejpb.2018.10.017

71. Shah HS, Joshi SA, Haider A, Kortz U, Iqbal J, Iqbal J. Synthesis of chitosan-coated polyoxometalate nanoparticles against cancer and its metastasis. *RSC Adv*. 2015;5(113):93234–93242. doi:10.1039/C5RA18489D

72. Croce M, Conti S, Maake C, Patzke GR. Nanocomposites of polyoxometalates and chitosan-based polymers as tuneable anticancer agents. *Eur J Inorg Chem*. 2019;2019(3–4):348–356. doi:10.1002/ejic.201800268

73. Pérez-álvarez L, Ruiz-Rubio L, Artetxe B, dM Vivanco M, Gutiérrez-Zorrilla JM, Vilas-Vilela JL. Chitosan nanogels as nanocarriers of polyoxometalates for breast cancer therapies. *Carbohydr Polym*. 2019;213:159–167. doi:10.1016/j.carbpol.2019.02.091

74. Wang X, Liu J, Pope M. New polyoxometalate/starch nanomaterial: synthesis, characterization and antitumoral activity. *Dalton Trans*. 2003;2003(5):957–960. doi:10.1039/b300920n

75. Razavi SF, Bamoharram FF, Hashemi T, Shahrokhabadi K, Davoodnia A. Nanolipid-loaded Preyssler polyoxometalate: synthesis, characterization and invitro inhibitory effects on HepG2 tumor cells. *Toxicol in vitro*. 2020;68:104917. doi:10.1016/j.tiv.2020.104917

76. Li X-H, Chen W-L, Wei M, et al. Polyoxometalates nanoparticles improve anti-tumor activity by maximal cellular uptake. *Inorganica Chim Acta*. 2019;486:104–112. doi:10.1016/j.ica.2018.10.046

77. Adan A, Kiraz Y, Baran Y. Cell proliferation and cytotoxicity assays. *Current Pharm Biotechnol*. 2016;17(14):1213–1221. doi:10.2174/1389201017666160808160513

78. Vijayan S, Divya K, Jisha M. In vitro anticancer evaluation of chitosan/biogenic silver nanoparticle conjugate on Si Ha and MDA MB cell lines. *Appl Nanosci*. 2020;10(3):715–728. doi:10.1007/s13204-019-01151-w

79. Allaoui A, Gascón S, Benomar S, et al. Protein hydrolysates from fenugreek (Trigonella foenum graecum) as nutraceutical molecules in colon cancer treatment. *Nutrients*. 2019;11(4):724. doi:10.3390/nu11040724

80. Almalki DA, Naguib DM. Anticancer activity of aqueous fenugreek seed extract against pancreatic cancer, histological evidence. *J Gastrointestinal Cancer*. 2022;53(3):683–686. doi:10.1007/s12029-021-00687-x

81. Kemp JA, Shim MS, Heo CY, Kwon YJ. "Combo" nanomedicine: co-delivery of multi-modal therapeutics for efficient, targeted, and safe cancer therapy. *Adv Drug Delivery Rev*. 2016;98:3–18. doi:10.1016/j.addr.2015.10.019

82. Habib I, Chohan TA, Chohan TA, et al. Integrated Computational Approaches for Designing Potent Pyrimidine-Based CDK9 Inhibitors: 3D-QSAR, Docking, and Molecular Dynamics Simulations. *Comput Biol Chem*. 2024;108:108003. doi:10.1016/j.compbiolchem.2023.108003

83. Hamza S, Abid A, Khanum A, et al. 3D-QSAR, docking and molecular dynamics simulations of novel Pyrazolo-pyridazinone derivatives as covalent inhibitors of FGFR1: a scientific approach for possible anticancer agents. *J Biomol Struct Dyn*. 2023;2023:1–15.

84. Khalid A, Afzal S, Abbas F, et al. Phytochemical, biological, and in-silico analysis of Colutea armata Hemsl. & Lace.: a possible source of bioactive natural compounds. *S Afr J Bot*. 2023;158:133–141. doi:10.1016/j.sajb.2023.05.003

85. Raza A, Chohan TA, Sarfraz M, et al. Molecular modeling of pyrrolo-pyrimidine based analogs as potential FGFR1 inhibitors: a scientific approach for therapeutic drugs. *J Biomol Struct Dyn*. 2023;41:1–14.

86. Rehman K, Chohan TA, Waheed I, Gilani Z, Akash MSH. Taxifolin prevents postprandial hyperglycemia by regulating the activity of α-amylase: evidence from an in vivo and in silico studies. *J Cell Biochem*. 2019;120(1):425–438. doi:10.1002/jcb.27398

87. Saleem H, Maqbool Khan K, Nadeem F, et al. Biochemical, Toxicological, and in-silico Aspects of Trillium govanianum Wall. ex D. Don (Trilliaceae): a Rich Source of Natural Bioactive Compounds. *Chem Biodivers*. 2023;21:e202301375.

88. Çankaya N, Izdal M, Azarkan SY. Synthesis, Characterization, Biological Evaluation and Molecular Docking Studies of New Oxoacrylate and Acetamide on HeLa Cancer Cell Lines. *Current Computer-Aided Drug Design*. 2021;17(6):838–848. doi:10.2174/1573409916666200907160434

89. Mahnashi MH, Alqahtani YS, Alyami BA, et al. Cytotoxicity, anti-angiogenic, anti-tumor and molecular docking studies on phytochemicals isolated from Polygonum hydropiper L. *BMC Complement Med Therap*. 2021;21:1–14. doi:10.1186/s12906-021-03411-1

90. Chohan TA, Chen -J-J, Qian H-Y, Pan Y-L, Chen J-Z. Molecular modeling studies to characterize N-phenylpyrimidin-2-amine selectivity for CDK2 and CDK4 through 3D-QSAR and molecular dynamics simulations. *Mol Biosyst*. 2016;12(4):1250–1268. doi:10.1039/C5MB00860C